Effect of iron vacancies on magnetic order and spin dynamics of the spin ladder $BaFe_{2-\delta}S_{1.5}Se_{1.5}$

Zengjia Liu,[1,*] Xiao-Sheng Ni,[1,*] Lisi Li,[1] Hualei Sun,[1] Feixiang Liang,[1] Benjamin A. Frandsen,[2]
Andrew D. Christianson,[3] Clarina dela Cruz,[3] Zhijun Xu,[4,5] Dao-Xin Yao,[1] Jeffrey W. Lynn,[4] Robert J. Birgeneau,[6,7]
Kun Cao,[1,†] and Meng Wang[1,‡]
[1]*Center for Neutron Science and Technology, Guangdong Provincial Key Laboratory of Magnetoelectric Physics and Devices,*
School of Physics, Sun Yat-Sen University, Guangzhou 510275, China
[2]*Department of Physics and Astronomy, Brigham Young University, Provo, Utah 84602, USA*
[3]*Materials Science and Technology Division, Oak Ridge National Laboratory, Oak Ridge, Tennessee 37831, USA*
[4]*NIST Center for Neutron Research, National Institute of Standards and Technology, Gaithersburg, Maryland 20899, USA*
[5]*Department of Materials Science and Engineering, University of Maryland, College Park, Maryland 20742, USA*
[6]*Department of Physics, University of California, Berkeley, California 94720, USA*
[7]*Materials Science Division, Lawrence Berkeley National Laboratory, Berkeley, California 94720, USA*

(Received 13 January 2022; revised 14 May 2022; accepted 1 June 2022; published 13 June 2022)

Quasi-one-dimensional iron chalcogenides possess various magnetic states depending on the lattice distortion, electronic correlations, and presence of defects. We present neutron diffraction and inelastic neutron scattering experiments on the spin ladder compound $BaFe_{2-\delta}S_{1.5}Se_{1.5}$ with ~6% iron vacancies. The data reveal that long-range magnetic order is absent, while the characteristic magnetic excitations that correspond to both the stripe- and block-type antiferromagnetic correlations are observed. First-principles calculations support the existence of both stripe- and block-type antiferromagnetic short-range orders in the experimental sample. The disappearance of long-range magnetic order may be due to the competition between these two magnetic orders, which is greatly enhanced for a certain concentration of iron vacancies, which we calculate to be about 6%, consistent with the measured iron vacancy concentration. Our results highlight how iron vacancies in the iron-based spin ladder system strongly influence the magnetic ground state.

DOI: 10.1103/PhysRevB.105.214303

I. INTRODUCTION

The mechanism of high-temperature superconductivity (SC) has remained a puzzle since the initial discovery of copper-based high-temperature superconductors [1]. SC emerges for both the copper- and iron-based families of superconductors upon the suppression of antiferromagnetic (AFM) order through charge doping or pressure [2–7]. AFM spin fluctuations have been put forth as an essential ingredient for high-temperature superconductivity [8]. Recently, pressure-induced superconductivity was found in the quasi-one-dimensional (quasi-1D) iron-based spin ladder compounds $BaFe_2X_3$ ($X = $ S, Se), placing the 1D Fe spin ladder systems into the iron-based superconductor family [9–11]. In contrast to the metallic parent compounds of the layered iron-based superconductors, both $BaFe_2S_3$ and $BaFe_2Se_3$ are insulating. It is speculated that the origin of superconductivity may be tied to a bandwidth-controlled Mott transition resulting from the increased transfer of Fe 3*d* electrons across the interladder bonds. These findings have prompted extensive experimental and theoretical research to determine the role of magnetism in the superconducting spin ladder compounds and their connection to the layered cuprates and iron chalcogenide superconductors [12–24].

The two end members of the $BaFe_2S_{3-x}Se_x$ phase diagram possess distinct crystal and magnetic structures. $BaFe_2S_3$ crystallizes into an orthorhombic structure with space group *Cmcm*, as shown in Fig. 1. The Fe atoms exhibit a stripe AFM ground state [17,25–27]. In contrast, $BaFe_2Se_3$ crystallizes a lower-symmetry orthorhombic space group *Pnma* in which the Fe ladders are slightly tilted [17,26–28]. The Fe magnetic moments order into a block AFM ground state, as shown in Fig. 1(c). To understand the evolution of the magnetic ground state in $BaFe_2S_{3-x}Se_x$ as a function of chemical substitution and pressure close to superconductivity, systematic neutron diffraction investigations have been conducted under ambient [27,29,30] and applied pressure [21,31]. The block AFM order is robust up to 6.8 GPa at 120 K in $BaFe_2Se_3$ [29]. With S substitution on Se sites, the block AFM order survives until approximately a 1:2 ratio of Se to S, at which point stripe AFM order appears [27,32]. Interestingly, short-range correlations of both the block and stripe types have been observed in the same sample of $BaFe_2S_2Se$, suggesting a nontrivial intermediate state between the long-range-order versions of the two magnetic ground states [27].

Anderson localization induced by the S and Se substitution is suggested to be crucial for the appearance of superconductivity in the 1D ladder system [33]. Disorder also influences the magnetic properties. In particular, the magnetic order is

---

[*] These authors contributed equally to this work.

[†] caok7@mail.sysu.edu.cn

[‡] wangmeng5@mail.sysu.edu.cn

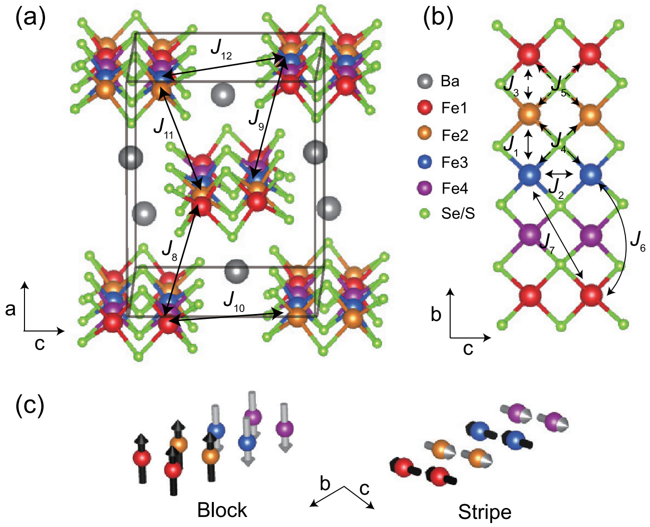

FIG. 1. (a) Visualization of the crystal structure of $BaFe_2S_{1.5}Se_{1.5}$. (b) Structure of an individual FeX ($X = S/Se$) ladder. J_1–J_{12} represent the magnetic exchange interactions between the marked magnetic ions. (c) Diagram of block and stripe antiferromagnetic orders. The directions of the magnetic moments are represented by the black and gray arrows.

highly sensitive to iron vacancies, as demonstrated by the spin-glass-like behavior observed in $BaFe_{1.8}Se_3$ [34] and the suppression of block-type long-range magnetic order by 4% iron vacancies in $BaFe_{2-\delta}S_{1.5}Se_{1.5}$ and 2% iron vacancies in $BaFe_{2-\delta}S_{0.67}Se_{2.33}$ [27]. The destruction of long-range magnetic order with such low concentrations of magnetic vacancies underscores the sensitive interplay between the magnetic interactions and detailed atomic structure in the Fe ladder system. To our knowledge, no deep understanding of the effect of iron vacancies on the magnetic ground state has been achieved, yet it may be related to the superconducting mechanism under high pressure. Hence, it is necessary to elucidate the role of iron vacancies in determining the magnetic ground state.

In this paper, we investigate the magnetic order and spin dynamics of $BaFe_{2-\delta}S_{1.5}Se_{1.5}$ with 6% Fe vacancies. Neutron powder diffraction (NPD) measurements demonstrate that no long-range magnetic order develops, although short-range block AFM correlations are observed at low temperature. Inelastic neutron scattering (INS) reveals the existence of both block- and stripe-type magnetic excitations, indicative of competition between these two types of magnetic orders. Using density functional theory (DFT), we calculated the magnetic ground state of $BaFe_{2-\delta}S_{1.5}Se_{1.5}$ for a range of iron vacancy concentrations. We find that a paramagnetic ground state can be ruled out for iron vacancy concentrations below 10%. The calculated ground state for the vacancy-free compound is the block AFM state, in agreement with experiments [27,32]. However, the relative energy of the stripe AFM state decreases with increasing iron vacancies, eventually becoming more energetically favorable than the block state for vacancy concentrations above ∼6%. Combined with our experimental observations, we thus conclude that the magnetic ground state of our sample consists of both the stripe and block AFM short-range orders. The disappearance of long-range magnetic order at such a low concentration of iron vacancies appears to be caused by the competition between the two types of magnetic order, which is greatly enhanced with the introduction of iron vacancies.

II. EXPERIMENTAL AND THEORETICAL METHODS

Single crystals with the nominal composition of $BaFe_2S_{1.5}Se_{1.5}$ were grown by the Bridgman method [27,35–37]. A sample of single crystals weighing 2.55 g total was ground into powder for neutron scattering experiments. The NPD experiment was conducted on the HB-2A instrument at the High Flux Isotope Reactor, Oak Ridge National laboratory (HFIR, ORNL) using a monochromatic beam with a wavelength of $\lambda = 2.4105$ Å. The powder diffraction patterns were refined by the Rietveld method using the FULLPROF SUITE [38,39]. Neutron diffraction measurements on single crystals were carried out on the BT7 thermal triple-axis spectrometer at the NIST Center for Neutron Research [40]. A closed-cycle refrigerator was used to control the sample temperature. The INS experiment was carried out on the wide angular-range time-of-flight chopper spectrometer (ARCS) at the Spallation Neutron Source (SNS), ORNL. The measurements were conducted at 5 K with incident beam energies of $E_i = 20$ and 150 meV. The corresponding energy resolutions were $\Delta E = 1.0$ and 7.0 meV, respectively, as determined by the full width at half maximum of the energy cuts at $\Delta E = 0$ meV. The SPINW program was utilized to simulate INS spectra and compare with the experimental results [41]. Magnetic susceptibility and resistivity measurements were performed using a physical property measurement system (Quantum Design). Energy-dispersive x-ray spectroscopy (EDS; EVO, Zeiss) was employed to determine the composition of the crystals.

First-principles calculations were carried out with the Vienna Ab initio Simulation Package (VASP) based on density functional theory [42,43]. We used the Perdew-Burke-Ernzerhof functional with a spin-polarized generalized gradient approximation (GGA). The projector augmented-wave [44] method with a 500 eV plane-wave cutoff was used, and a $6 \times 4 \times 4$ Monkhorst-Pack k-point mesh allowed the calculation to converge well. The spin-polarized GGA we used was combined with on-site Coulomb interactions U, included for Fe $3d$ orbitals (GGA $+U$) [45]. We employed $U = 1$ eV and $J = 0.4$ eV, which achieved values of the magnetic moments and band gap that are consistent with experiments. We started with the experimental atomic structure and then relaxed the crystal structure until the forces acting on each atom were less than 1 meV/Å. In order to simulate the S substitution of Se, we employed the virtual crystal approximation [46] for the same atomic coordinates of Se and S atoms. The supercell we used is a monoclinic crystal cell with 32 Fe atoms, which can accommodate both the block and stripe AFM orders. For the block AFM order, the Fe1 and Fe2 spins have the same orientation, while the Fe3 and Fe4 spins are antiparallel to Fe1 and Fe2. For the stripe AFM order, Fe1 and Fe4 spins have the same orientation, opposite the Fe2 and Fe3 spins [see Fig. 1(c)]. The effect of iron vacancies was

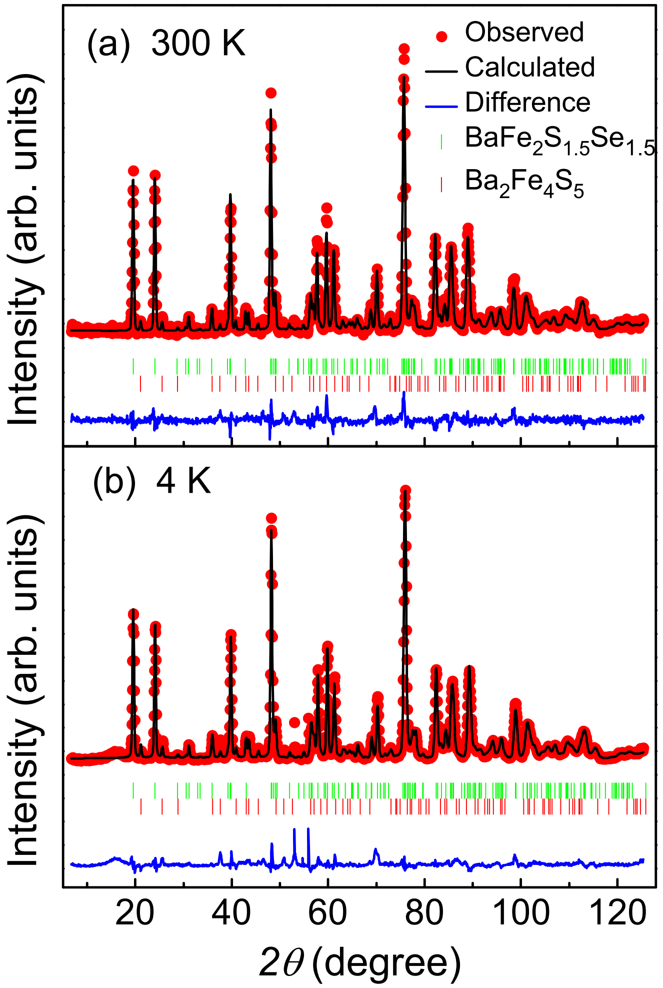

FIG. 2. Observed and calculated neutron powder diffraction patterns for $BaFe_2S_{1.5}Se_{1.5}$ at 300 and 4 K. Small impurity peaks corresponding to $Ba_2Fe_4S_5$ are observed.

modeled by removing a given number of randomly selected Fe atoms from the supercell, calculating the results, and then averaging the results with those from equivalent calculations performed with the same number of iron atoms removed from other randomly selected positions.

III. RESULTS AND DISCUSSION

Figure 2 shows NPD patterns for $BaFe_{2-\delta}S_{1.5}Se_{1.5}$ measured at 4 and 300 K. Small impurity peaks corresponding to $Ba_2Fe_4S_5$ were observed. No sharp magnetic peaks are seen in the NPD pattern at 4 K, in clear contrast to our previous measurements on as-grown powder samples with the same nominal composition, where there are strong magnetic peaks corresponding to the block AFM order at low temperature [27]. The weak, broad feature centered around $2\theta = 16.5^\circ$ in Fig. 2(b) corresponds to block-type short-range magnetic order at $Q = (H, K, L) = (0.5, 0.5, 0.5)$. Here, (H, K, L) are Miller indices for the momentum transfer $|Q| = 2\pi\sqrt{(H/a)^2 + (K/b)^2 + (L/c)^2}$, where the lattice constants and refined structural parameters are listed in Table I. The space group *Pnma* agrees with previous reports. The structural refinement reveals the presence of ∼6% iron vacancies, corresponding to a refined composition of $BaFe_{1.89(2)}S_{1.5(1)}Se_{1.5(1)}$. We note that the ratio of the S and Se atoms varies depending on the atomic site. The composition determined from EDS, normalized by the Ba content, is $Ba_{1.00(5)}Fe_{1.92(9)}S_{1.38(12)}Se_{1.37(15)}$.

TABLE I. The refined structural parameters for the sample with the nominal composition $BaFe_2S_{1.5}Se_{1.5}$ determined from NPD data at 4 K (goodness of fit $\chi^2 = 19.5$, $R_p = 13.9\%$, $R_{wp} = 16.3\%$, and $R_{\text{exp}} = 3.7\%$).

Parameter	Value	
Crystal system	Orthorhombic	
Space group	*Pnma*	
Unit cell parameters	$a = 11.5480(4)$Å	
	$b = 5.3208(1)$Å	
	$c = 8.9910(3)$Å	
	$\alpha = \beta = \gamma = 90^\circ$	
Atomic parameters	(x, y, z)	Occupancy
Ba	(0.1919,0.25,0.524)	0.50
Fe	(0.4936,0.0017,0.3506)	0.945(9)
Se1	(0.3530,0.25,0.233)	0.22(2)
Se2	(0.623, 0.25, 0.491)	0.14(1)
Se3	(0.3999,0.25,0.8193)	0.40(2)
S1	(0.3530,0.25,0.233)	0.28(2)
S2	(0.623,0.25,0.491)	0.36(1)
S3	(0.3999,0.25,0.8193)	0.10(2)

To gain more insight into the short-range magnetic structure, we conducted neutron diffraction measurements on a single-crystal sample. The data shown in Figs. 3(a)–3(d) reveal the appearance of broad magnetic peaks centered at $Q = (0.5, 1.0, 0.5)$ and $Q = (0.5, 0.5, 0.5)$, corresponding to the stripe and block AFM orders, respectively. Considering that these magnetic peaks were not observable in the powder samples, instead requiring a large single crystal and the high flux at BT7 for unambiguous observation, the magnetic order is expected to be weak and short range. The domain size of the stripe AFM order along the leg direction was determined to be ∼47 Å by convoluting the instrumental resolution. The temperature-dependent resistivity shown in Fig. 3(e) exhibits insulating behavior, consistent with the other compositions in this system [27,32]. The temperature-dependent magnetic susceptibility in Fig. 3(f) displays kinks at 39 and 116 K, indicating multiple magnetic transitions. However, the neutron diffraction intensity measured at $Q = (0.5, 0.5, 0.5)$ (corresponding to the block AFM order) shows a broad transition beginning at 81 K. These results suggest that the transition temperature may depend on the resolution and sensitivity of the instrument, as in a short-range cluster spin glass system [47]. To investigate the magnetic correlations present at low temperature, we conducted INS measurements on the same powder sample. Figures 4(a) and 4(b) display the INS spectra with incident energies of $E_i = 20$ and 150 meV, respectively. The experimentally observed INS spectra include spin excitations and phonons from the sample and sample holder. We could identify the contributions from spin excitations based on the wave vectors and dispersions. Intense gapless magnetic excitations can be observed at low Q in Fig. 4(a).

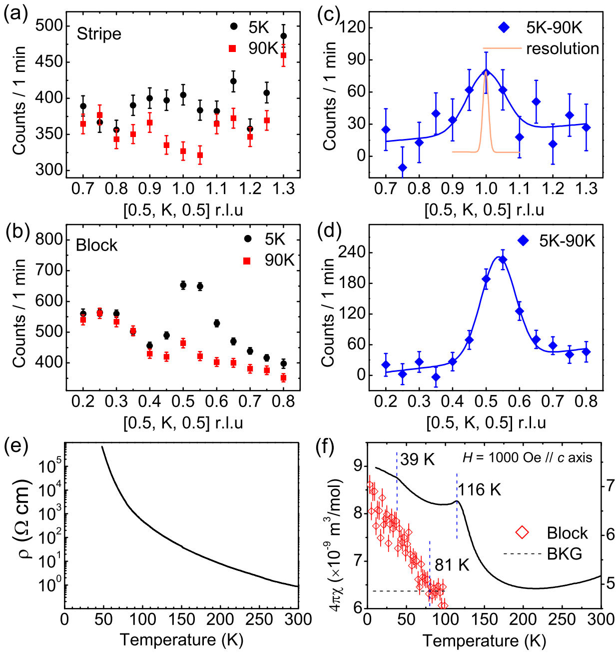

FIG. 3. Elastic scans along the $(0.5, K, 0.5)$ direction across (a) $K = 1$ and (b) $K = 0.5$ at 5 and 90 K. (c) and (d) The temperature differences between 5 and 90 K for $K = 1$ and $K = 0.5$, respectively. The solid lines are Gaussian fits to the data. The bars in (a)–(d) represent the statistical errors that correspond to one standard deviation. The instrumental resolution at $Q = (0.5, 1.0, 0.5)$ was determined by measuring the nuclear Bragg peak of $Q = (1, 2, 1)$. (e) Resistivity measured as a function of temperature. (f) Magnetic susceptibility measured with a 1000 Oe magnetic field parallel to the b axis. The dashed lines mark kinks at 39 and 116 K. The open red diamonds show the temperature dependence of the block AFM magnetic order parameter measured at $Q = (0.5, 0.5, 0.5)$. The order parameter reaches the background (BKG) at 81 K.

Representative constant energy cuts at $E = 2$, 4, 6 meV and constant Q cuts at $Q = 4.75$ and 5.75 Å^{-1} are plotted in Figs. 4(e) and 4(f). Two magnetic excitation modes centered at $Q = 0.75$ and 1.26 Å^{-1} can be identified in Fig. 4(e). The excitation mode at $Q = 0.75$ Å^{-1} is ascribed to the block AFM order at the wave vector (0.5, 0.5, 0.5) [17]. The mode at $Q = 1.26$ Å^{-1} is consistent with the stripe AFM wave vector at (0.5, 1.0, 0.5), like that observed in $BaFe_2S_3$ [26]. Thus, the spin excitations measured by INS demonstrate that both the block and stripe AFM correlations exist in $BaFe_{1.89}S_{1.5}Se_{1.5}$. The magnetic excitations at higher energies in Figs. 4(b) and 4(f) show broad features, consistent with short-range magnetic correlations.

Using a classical Heisenberg model, we can describe the magnetic interactions in $BaFe_{1.89}S_{1.5}Se_{1.5}$ with the magnetic Hamiltonian

$$H_{\rm spin} = \sum_{i<j} J_{ij}\mathbf{S}_i \cdot \mathbf{S}_j, \qquad (1)$$

where the sum runs over magnetic atoms in the compound and J_{ij} are exchange integrals between Fe spins S_i and S_j. To describe correctly the magnetic configurations of this system, both intraladder and interladder interactions should be considered. Here, we include 12 nonequivalent exchange interactions with bond lengths less than 7 Å, labeled J_1 through J_{12}, which we illustrate in Figs. 1(a) and 1(b). Among the 12 J's, J_1–J_7 are intraladder interactions, and the rest are interladder interactions. Our choice of the 12 nonequivalent J's contains all the corresponding J's in Ref. [17], in which eight exchange parameters were chosen to describe magnetic interactions in $BaFe_2Se_3$. The number of J's increases in the present system because of the lower symmetry. We determined the values of these interactions by fitting all 12 J parameters to the magnetic energies calculated by DFT using 50 randomly generated collinear (RGC) magnetic

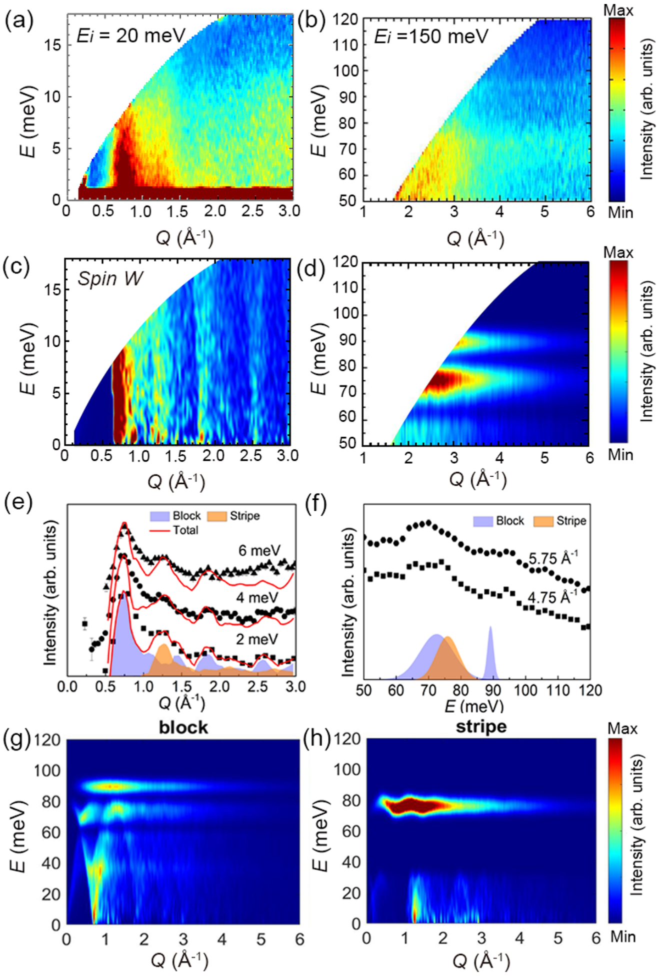

FIG. 4. INS spectra $S(Q, \omega)$ for $BaFe_{1.89}S_{1.5}Se_{1.5}$ at 5 K with (a) $E_i = 20$ and (b) 150 meV. Calculated $S_{\rm SWT}(Q, \omega)$ using linear spin wave theory for (c) $E_i = 20$ and (d) 150 meV with intensities from the block and stripe AFM orders in a ratio of 4:1. The calculations include a convolution with the energy resolution of 1 and 7 meV for $E_i = 20$ meV and $E_i = 150$ meV, respectively. (e) Constant-energy cuts through $S(Q, \omega)$ integrated over energy intervals of 2 ± 0.5, 4 ± 0.5, and 6 ± 0.5 meV using $E_i = 20$ meV. The black dots are the experimental results, and the red curves represent the simulation. (f) Constant-momentum cuts through $S(Q, \omega)$ integrated over 4.75 ± 0.25 and 5.75 ± 0.25 Å^{-1}. In (e) and (f), the shaded regions represent the calculated magnetic excitation intensities from the block and stripe AFM orders for the same ratio as in (c) and (d). (g) and (h) The powder-averaged calculated spin excitation spectra for the block and stripe magnetic orders, respectively.

configurations [48,49]. The resulting values of SJ_1 through SJ_{12} are −21.7, −24.6, 21.2, 25.5, 40.4, 9.3, 4.2, 0.5, 0.8, 3.8, 0.4, and 0.7 meV, where S is assumed to be 2. Our calculated results are generally consistent with those in Ref. [17]. Specifically, to form a block magnetic state, J_1 and J_3 should be different in sign, which is consistent with the corresponding SJ_1 and SJ_1' in Ref. [17]. We also find that $SJ_2 = 11$ meV and $SJ_2' = 6$ meV in Ref. [17], with a similar ratio between the corresponding J_4 and J_5 interactions found in our results. It is worth noting that $\mathrm{BaFe_{2-\delta}S_{1.5}Se_{1.5}}$ is a compound with a different atomic structure and symmetry than $\mathrm{BaFe_2Se_3}$. It would be difficult to compare J's between these two systems cleanly. However, given that the ground state of vacancy-free $\mathrm{BaFe_{2-\delta}S_{1.5}Se_{1.5}}$ is the block magnetic phase observed in $\mathrm{BaFe_2Se_3}$, it is reasonable to suppose that the exchange interactions in these two compounds could share some common features. To further check the completeness of our choice of J's, we performed calculations on another 60 RGC spin configurations. The fitted values for the 12 exchange integrals were then substituted into Eq. (1), and the energy, $E_{\mathrm{Heisenberg}}$, was calculated for each of the 60 RGC spin configurations. In Fig. 5(a), we compare $E_{\mathrm{Heisenberg}}$ to the energies obtained from *ab initio* calculations, $\mathrm{E}_{ab\ initio}$, using the same 60 RGC spin configurations. Each black circle represents one of the RGC configurations, and they all lie very close to the line $E_{\mathrm{Heisenberg}} = E_{ab\ initio}$ shown in red. This close agreement demonstrates the completeness of our choice of exchange interactions in $\mathrm{BaFe_{1.89}S_{1.5}Se_{1.5}}$.

With the calculated magnetic exchange integrals, we can simulate the spin wave spectra in linear spin wave theory using the SPINW software package [41]. The six most prominent magnetic exchange interactions, SJ_{1-6}, are included in the simulations of the powder-averaged magnetic spin excitation spectra of the block and stripe AFM orders. The other calculated magnetic couplings are below 5 meV and would have negligible observable impact on the spin wave spectra. In Figs. 4(c)–4(f), we reproduce the spin wave spectra of $\mathrm{BaFe_{1.89}S_{1.5}Se_{1.5}}$ by combining the block AFM and stripe AFM excitations with spectral weights of 80% and 20%, respectively. The greater width of the observed spin excitations compared to the calculations results from the short-range magnetic order in the sample, as opposed to conventional long-range order. We note that, theoretically, one set of magnetic couplings would result in a degenerate magnetic ground state. Small deviations of the magnetic couplings could result in different magnetic orders. However, their effect on the magnetic excitation spectra may be negligible given a specific magnetic order.

To explore the effect of iron vacancies on the magnetic properties, we performed DFT calculations for $\mathrm{BaFe_{2-\delta}S_{1.5}Se_{1.5}}$ in the paramagnetic (PM) phase, block AFM phase, and stripe AFM phase with varying amounts of iron vacancies. First, we must define an appropriate model for the PM phase. Here, we employed the magnetic sampling method (MSM). Within the Heisenberg model, a PM phase can be modeled by averaging multiple spin configurations in such a way that individual exchange interactions cancel, i.e., $\varphi = \sum_k \langle S_i(k)\ S_j(k)\rangle = 0$, where k denotes the spin configuration. This MSM method has been reliably used to model the PM phase of $\mathrm{ZnCr_2O_4}$ [50] and $\mathrm{CaBaCo_4O_7}$ [51]. If we consider the 12 inequivalent exchange interactions, the PM phase in $\mathrm{BaFe_{2-\delta}S_{1.5}Se_{1.5}}$ can be modeled with four collinear spin configurations, resulting in vanishing exchange integrals between the Fe spins. To validate this approach, we performed calculations on 100 RGC spin configurations, whose average energy is representative of the energy of the PM phase. In Fig. 5(b), we plot the individual energies of the 100 RGC spin configurations (black dots) and their cumulative average (red curve) relative to the average energy of the four spin configurations selected for the PM model (green dashed line). The cumulative average energy of 100 RGC spin configurations converges to the energy from the four spin configurations representing the PM phase.

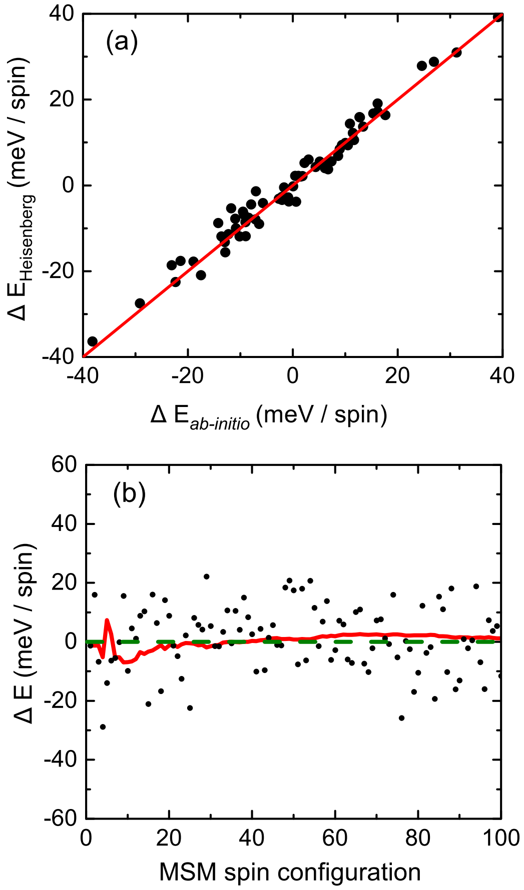

FIG. 5. (a) The energies of 60 RGC spin configurations calculated via *ab initio* methods versus the Heisenberg equation [Eq. (1)] using the 12 fitted exchange interactions described in the text. The solid red line shows the equation $E_{\mathrm{Heisenberg}} = E_{ab\ initio}$. (b) *Ab initio* calculated energy of 100 RGC spin configurations (black points) with the corresponding accumulated average (red solid line) compared to the average energy of the four spin configurations (green dashed line) used to approximate the PM phase.

Having verified our model for the PM phase, we then calculated the total magnetic energy of $\mathrm{BaFe_{2-\delta}S_{1.5}Se_{1.5}}$ in the block AFM, stripe AFM, and PM phases as a function of iron vacancy concentration. Our theoretical calculations involve comparisons of energies alone. There is no entropy; that is, the calculations correspond to $T = 0$ even for the PM phase. Figure 6(a) shows the results calculated using the experimentally refined parameters in Table I without

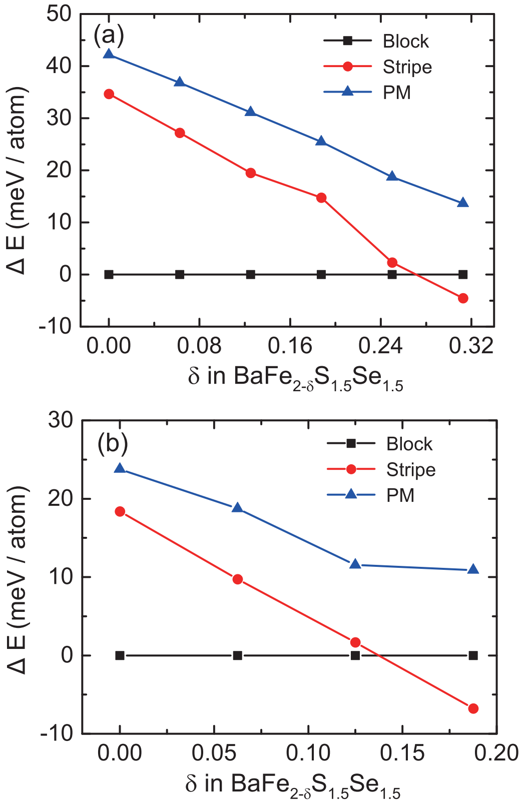

FIG. 6. Variation of the block AFM, stripe AFM, and PM ground state energies (relative to the block AFM energy) as a function of iron vacancy concentration (a) without geometry optimization and (b) with geometry optimization.

geometry and atomic position optimization. The total energy of the PM phase is always well above the other two phases and thus can be ruled out as the ground state. The block AFM phase is more stable than the stripe AFM phase when the Fe vacancy concentration is less than 12%, above which the trend reverses. The introduction of Fe vacancies may affect the atomic configurations, so we also performed equivalent calculations with geometry and atomic position optimization, with the corresponding results shown in Fig. 6(b). In this case, the crossing point between the block AFM and stripe AFM phases is shifted to ∼6%, which is very close to the vacancy concentration in the present sample. Although it is not possible for us to fine-tune the concentration of Fe vacancies in the DFT calculations due to the limitations of the supercell size and computational power, the calculated results clearly show that the competition between these two phases can be tuned by iron vacancies. Within a certain range of the vacancy concentrations around 6%, the competition of these two phases may become so strong that the long-range order is destroyed, consistent with the sample used in the present study. Microscopically, the disappearance of long-range magnetic order might also be caused by the dilution of exchange interactions due to the introduction of Fe vacancies, similar to the percolation effect in diluted magnetic semiconductors. However, such an effect typically requires a vacancy concentration well above 10%. This dilution effect may explain the absence of the block AFM order in severely iron deficient $BaFe_{1.8}Se_3$ [34].

For a realistic sample, one would not expect the composition to exactly locate at the magic concentration where the energies of the two magnetic orders are equal. As the temperature is lowered, the regions with different Fe-vacancy contractions and therefore different preferred phases (block or stripe) would freeze out so that they are simply not able to come to equilibrium with each other. Further, as the clusters freeze, they will tend to exert random magnetic fields on each other, thus enhancing the spin disorder and causing the time to equilibrate and to diverge exponentially with decreasing temperature, forming a novel spin glass state with two short-range orders. In other words, the disorder is ultimately a kinetic phenomenon with the system unable to find its true ground state, regardless of whether it is stripe or block.

IV. SUMMARY

In summary, we have measured the short-range magnetic order and spin excitation spectrum of coexisting short-range stripe and block AFM orders in quasi-one-dimensional $BaFe_{1.89}S_{1.5}Se_{1.5}$. The iron vacancies are implicated in the lack of long-range magnetic order in the ground state and the existence of both stripe- and block-type excitation modes. First-principles calculations have confirmed the competition between stripe and block AFM orders, with maximum concentration expected around an iron vacancy concentration of ∼6%, very close to the actual composition of the sample used in the present work. Our findings highlight the unusual sensitivity of the magnetic ground state to the presence of iron vacancies in the quasi-1D spin ladder system $BaFe_2(S,Se)_3$. These results are expected to be relevant for other pressure-induced superconductors in the family of quasi-1D iron pnictide and selenide systems.

ACKNOWLEDGMENTS

Work at Sun Yat-Sen University was supported by the National Natural Science Foundation of China (Grants No. 11904414, No. 12174454, No. 11904416, and No. 11974432), the Guangdong Basic and Applied Basic Research Foundation (Grants No. 2021B1515120015 and No. 2019A1515011337), and the National Key Research and Development Program of China (Grants No. 2019YFA0705702, No. 2018YFA0306001, and No. 2017YFA0206203). Work at the University of California, Berkeley, and Lawrence Berkeley National Laboratory was funded by the U.S. Department of Energy, Office of Science, Office of Basic Energy Sciences, Materials Sciences and Engineering Division under Contract No. DE-AC02-05-CH11231 within the Quantum Materials Program (KC2202) and the Office of Basic Energy Sciences. A.D.C. was partially supported by the U.S. Department of Energy, Office of Science, Basic Energy Sciences, Materials Science and Engineering Division. The experiment at Oak Ridge National Laboratory's Spallation Neutron Source was sponsored by the Scientific User Facilities Division, Office of Basic Energy Sciences, U.S. Department of Energy.

[1] J. G. Bednorz and K. A. Müller, Z. Phys. B **64**, 189 (1986).
[2] Y. Kamihara, T. Watanabe, M. Hirano, and H. Hosono, J. Am. Chem. Soc. **130**, 3296 (2008).
[3] F.-C. Hsu, J.-Y. Luo, K.-W. Yeh, T.-K. Chen, T.-W. Huang, P. M. Wu, Y.-C. Lee, Y.-L. Huang, Y.-Y. Chu, D.-C. Yan, and M.-K. Wu, Proc. Natl. Acad. Sci. U.S.A. **105**, 14262 (2008).
[4] M. D. Lumsden and A. D. Christianson, J. Phys.: Condens. Matter **22**, 203203 (2010).
[5] B. Vignolle, S. Hayden, D. McMorrow, H. M. Rønnow, B. Lake, C. Frost, and T. Perring, Nat. Phys. **3**, 163 (2007).
[6] J. Paglione and R. L. Greene, Nat. Phys. **6**, 645 (2010).
[7] D. C. Johnston, Adv. Phys. **59**, 803 (2010).
[8] D. J. Scalapino, Rev. Mod. Phys. **84**, 1383 (2012).
[9] H. Takahashi, A. Sugimoto, Y. Nambu, T. Yamauchi, Y. Hirata, T. Kawakami, M. Avdeev, K. Matsubayashi, F. Du, C. Kawashima, H. Soeda, S. Nakano, Y. Uwatoko, Y. Ueda, T. J. Sato, and K. Ohgushi, Nat. Mater. **14**, 1008 (2015).
[10] T. Yamauchi, Y. Hirata, Y. Ueda, and K. Ohgushi, Phys. Rev. Lett. **115**, 246402(R) (2015).
[11] J. Ying, H. Lei, C. Petrovic, Y. Xiao, and V. V. Struzhkin, Phys. Rev. B **95**, 241109(R) (2017).
[12] G. R. Stewart, Rev. Mod. Phys. **83**, 1589 (2011).
[13] J. M. Caron, J. R. Neilson, D. C. Miller, K. Arpino, A. Llobet, and T. M . McQueen, Phys. Rev. B **85**, 180405(R) (2012).
[14] A. Krzton-Maziopa, E. Pomjakushina, V. Pomjakushin, D. Sheptyakov, D. Chernyshov, V. Svitlyk, and K. Conder, J. Phys.: Condens. Matter **23**, 402201 (2011).
[15] R. Arita, H. Ikeda, S. Sakai, and M.-T. Suzuki, Phys. Rev. B **92**, 054515 (2015).
[16] S. Dong, J.-M. Liu, and E. Dagotto, Phys. Rev. Lett. **113**, 187204 (2014).
[17] M. Mourigal, S. Wu, M. B. Stone, J. R. Neilson, J. M. Caron, T. M. McQueen, and C. I. Broholm, Phys. Rev. Lett. **115**, 047401 (2015).
[18] Y. Hirata, S. Maki, J.-i. Yamaura, T. Yamauchi, and K. Ohgushi, Phys. Rev. B **92**, 205109 (2015).
[19] D. Ootsuki, N. L. Saini, F. Du, Y. Hirata, K. Ohgushi, Y. Ueda, and T. Mizokawa, Phys. Rev. B **91**, 014505 (2015).
[20] M.-T. Suzuki, R. Arita, and H. Ikeda, Phys. Rev. B **92**, 085116 (2015).
[21] S. Chi, Y. Uwatoko, H. Cao, Y. Hirata, K. Hashizume, T. Aoyama, and K. Ohgushi, Phys. Rev. Lett. **117**, 047003 (2016).
[22] N. D. Patel, A. Nocera, G. Alvarez, A. Moreo, and E. Dagotto, Phys. Rev. B **96**, 024520 (2017).
[23] Y. Zhang, L.-F. Lin, J.-J. Zhang, E. Dagotto, and S. Dong, Phys. Rev. B **97**, 045119 (2018).
[24] S. Li, Y. Tang, T. A. Maier, and S. Johnston, Phys. Rev. B **97**, 195116 (2018).
[25] K. Klepp, W. Sparlinek, and H. Boller, J. Alloys Compd. **238**, 1 (1996).
[26] M. Wang, S. J. Jin, M. Yi, Y. Song, H. C. Jiang, W. L. Zhang, H. L. Sun, H. Q. Luo, A. D. Christianson, E. Bourret-Courchesne, D. H. Lee, D.-X. Yao, and R. J. Birgeneau, Phys. Rev. B **95**, 060502(R) (2017).
[27] J. Yu, M. Wang, B. A. Frandsen, H. Sun, J. Yin, Z. Liu, S. Wu, M. Yi, Z. Xu, A. Acharya, Q. Huang, E. Bourret-Courchesne, J. W. Lynn, and R. J. Birgeneau, Phys. Rev. B **101**, 235134 (2020).
[28] W. Zheng, V. Balédent, M.-B. Lepetit, P. Retailleau, E. V. Elslande, C. R. Pasquier, P. Auban-Senzier, A. Forget, D. Colson, and P. Foury-Leylekian, Phys. Rev. B **101**, 020101(R) (2020).
[29] S. Wu, J. Yin, T. Smart, A. Acharya, C. L. Bull, N. P. Funnell, T. R. Forrest, G. Simutis, R. Khasanov, S. K. Lewin, M. Wang, B. A. Frandsen, R. Jeanloz, and R. J. Birgeneau, Phys. Rev. B **100**, 214511 (2019).
[30] S. Wu, B. A. Frandsen, M. Wang, M. Yi, and R. Birgeneau, J. Supercond. Novel Magn. **33**, 143 (2020).
[31] L. Zheng, B. A. Frandsen, C. Wu, M. Yi, S. Wu, Q. Huang, E. Bourret-Courchesne, G. Simutis, R. Khasanov, D.-X. Yao, M. Wang, and R. J. Birgeneau, Phys. Rev. B **98**, 180402(R) (2018).
[32] F. Du, Y. Ueda, and K. Ohgushi, Phys. Rev. Lett. **123**, 086601 (2019).
[33] H. Sun, X. Li, Y. Zhou, J. Yu, B. A. Frandsen, S. Wu, Z. Xu, S. Jiang, Q. Huang, E. Bourret-Courchesne, L. Sun, J. W. Lynn, R. J. Birgeneau, and M. Wang, Phys. Rev. B **101**, 205129 (2020).
[34] B. Saparov, S. Calder, B. Sipos, H. Cao, S. Chi, D. J. Singh, A. D. Christianson, M. D. Lumsden, and A. S. Sefat, Phys. Rev. B **84**, 245132 (2011).
[35] C. Liu, J. L. Shen, J. C. Gao, C. J. Yi, D. Liu, T. Xie, L. Yang, S. Danilkin, G. C. Deng, W. H. Wang, S. L. Li, Y. G. Shi, H. M. Weng, E. K. Liu, and H. Q. Luo, Sci. China: Phys., Mech. Astron. **64**, 217062 (2021).
[36] H. Sun, C. Chen, Y. Hou, W. Wang, Y. Gong, and M. Huo, Sci. China: Phys., Mech. Astron. **64**, 118211 (2021).
[37] L. Li, X. Hu, Z. Liu, J. Yu, B. Cheng, S. Deng, L. He, K. Cao, D.-X. Yao, and M. Wang, Sci. China: Phys., Mech. Astron. **64**, 287412 (2021).
[38] J. Rodríguez-Carvajal, Phys. B (Amsterdam, Neth.) **192**, 55 (1993).
[39] The identification of any commercial product or trade name does not imply endorsement or recommendation by the National Institute of Standards and Technology.
[40] J. W. Lynn, Y. Chen, S. Chang, Y. Zhao, S. Chi, W. Ratcliff, B. G. Ueland, and R. W. Erwin, J. Res. Natl. Inst. Stand. Technol. **117**, 60 (2012).
[41] S. Toth and B. Lake, J. Phys.: Condens. Matter **27**, 166002 (2015).
[42] G. Kresse and J. Hafner, Phys. Rev. B **47**, 558 (1993).
[43] G. Kresse and J. Furthmüller, Phys. Rev. B **54**, 11169 (1996).
[44] P. E. Blöchl, Phys. Rev. B **50**, 17953 (1994).
[45] A. I. Liechtenstein, V. I. Anisimov, and J. Zaanen, Phys. Rev. B **52**, R5467 (1995).
[46] L. Bellaiche and D. Vanderbilt, Phys. Rev. B **61**, 7877 (2000).
[47] X. Lu, D. W. Tam, C. Zhang, H. Luo, M. Wang, R. Zhang, L. W. Harriger, T. Keller, B. Keimer, L.-P. Regnault, T. A. Maier, and P. Dai, Phys. Rev. B **90**, 024509 (2014).
[48] N. S. Fedorova, C. Ederer, N. A. Spaldin, and A. Scaramucci, Phys. Rev. B **91**, 165122 (2015).
[49] D. Morgan, B. Wang, G. Ceder, and A. van de Walle, Phys. Rev. B **67**, 134404 (2003).
[50] C. J. Fennie and K. M. Rabe, Phys. Rev. Lett. **96**, 205505 (2006).
[51] R. D. Johnson, K. Cao, F. Giustino, and P. G. Radaelli, Phys. Rev. B **90**, 045129 (2014).